A Generalized Theory of Ion Conductivity in Nanoporous Media

Jerry P. Owusu[1], Kevin M. Rosso[2], Russell L. Detwiler[1], and Mohammad Javad Abdolhosseini Qomi[1,3,4*]
[1]*Department of Civil and Environmental Engineering, University of California, Irvine, CA 92697, USA.*
[2]*Physical and Computational Sciences Directorate, Pacific Northwest National Laboratory, Richland, WA, USA.*
[3]*Department of Materials Science and Engineering, University of California, Irvine, CA 92697, USA. and*
[4]*Department of Mechanical and Aerospace Engineering, University of California, Irvine, CA 92697, USA.*
(Dated: March 26, 2026)

* E-mail: mjaq@uci.edu

I. ION DISTRIBUTION THROUGH NANOPORE

The spatial distributions of ions and water near charged and neutral nanopore surfaces reveal the interplay between surface ionophilicity, electrostatics, and interfacial structure (Figs. S1–S2). For neutral surfaces (Fig. S1), ion and water layering directly reflect surface ionophilicity: increasing ϵ_s/k_BT from 0.07 to 0.58 amplifies the primary water peak. It symmetrically enhances Na^+ and Cl^- accumulation in the first interfacial layer, with densities recovering bulk values beyond ~ 0.5 nm. Under surface charging, counterions (Na^+) accumulate within the electrical double layer with peak densities that grow with Σ_s and are further amplified at high ionophilicity (ϵ_s/k_BT=0.58), where electrostatic and van der Waals forces cooperatively promote cation adsorption; co-ions (Cl^-) are correspondingly depleted across the interfacial region. The primary water hydration peak also intensifies with surface charge, indicating stronger molecular alignment with the interfacial electric field.

Figure S8 reports the net interfacial ion charge density versus Σ_s for low and high ionophilicity. At high ionophilicity, all data lie above the unity line, indicating systematic overscreening: strong ion–surface van der Waals attractions favor counterion adsorption over competing water molecules, causing the first ion layer to overcompensate the surface charge and produce charge reversal [1, 2]. At low ionophilicity, reduced counterion adsorption yields underscreening at moderate Σ_s, with the net ionic charge remaining below the unity line; only at the highest surface charge does near-complete compensation emerge once electrostatic attraction overcomes weak dispersion forces and solvent crowding [2]. Thus, ionophilicity governs the onset of the underscreening-to-overscreening crossover and the strength of counterion correlations at the interface.

II. DIFFUSION COEFFICIENT CALCULATIONS AND FINITE-SIZE CORRECTIONS

A. Hydrodynamic Artifacts in Confined Systems

Initial diffusion measurements at the largest pore width (H=10 nm, Fig. S12d) yielded values exceeding the bulk diffusion coefficient D_0, an apparently counterintuitive enhancement arising from hydrodynamic finite-size effects under periodic boundary conditions. As shown by Simonnin *et al.* [3], periodic images introduce spurious hydrodynamic interactions that shift the measured diffusion coefficient away from its infinite-system limit, with the magnitude and sign of the correction depending on the aspect ratio H/L, where H is the pore height and L the lateral box dimension. For tall, narrow systems ($H > L$), the finite-size correction is positive ($\Delta D \propto +H/L^2$), so that $D_\infty = D_{\text{measured}} - \Delta D$ lies below the measured value; the measured diffusion can nonetheless exceed both the true confined value $D(H)$ and even D_0 when confinement-induced enhancement is present (Figs. S12e–f). Conversely, for flat, wide systems ($H < L$), the correction is negative ($\Delta D \propto -H/L^2$), meaning the infinite-system value exceeds the finite-size measurement and explaining why the apparent diffusion coefficient appears suppressed relative to the infinite lateral-size limit (Figs. S12a–c).

B. Extrapolation to Infinite Lateral Dimensions

Direct application of the Simonnin et al. [3] analytical corrections, derived for simple Lennard-Jones fluids with no-slip boundaries, proved inadequate for our complex electrolyte systems with strong interfacial layering and ion-specific surface interactions. We therefore adopted a systematic extrapolation approach: for each pore width H and surface condition, simulations were performed at progressively larger lateral box sizes L, and the parallel diffusion coefficient $D_\parallel(L)$ was computed as a function of $1/L^2$ and extrapolated to $L \to \infty$ using the hydrodynamic scaling identified by Simonnin et al. [3] (Figs. S12a–d). The resulting $D(H, L \to \infty)$ is taken as the physically meaningful, artifact-free diffusion coefficient. For the 5 and 10 nm pores ($H > L$), the extrapolated D_∞ falls below the finite-L values (Figs. S12e–f), whereas for narrower pores ($H \leq 3$ nm), D_∞ exceeds the finite-L result (Figs. S12a–c), consistent with the positive and negative ΔD corrections predicted by Simonnin et al. [3] as a function of H and L.

C. Theoretical Framework for Pore-Scale Diffusion

The slip-length parametrization commonly used in continuum hydrodynamics proves inadequate for electrolyte-filled nanopores, where dynamics are governed by spatially varying viscous forces and strong ion-specific surface adsorption. Building on classical activation energy theory and the frameworks of Simonnin *et al.* [3], and Saugey *et al.* [4], we decompose the pore-averaged diffusion coefficient D_p into bulk-like and surface contributions. The bulk-like term

accounts for confinement-induced suppression of long-wavelength hydrodynamic modes,

$$D_b = D_0(1 + 2\Gamma_c), \tag{1}$$

where Γ_c is a dimensionless confinement factor capturing the geometric effect of restricted perpendicular motion. Ion mobility near the interface is governed by an activation barrier set by surface ionophilicity,

$$D_s = -D_0\, 2\Gamma_c\Gamma_s, \tag{2}$$

where Γ_s quantifies the fraction of ions trapped in low-mobility interfacial layers via thermally activated surface binding, and Γ_c encodes the confinement geometry:

$$\Gamma_s = \exp\!\left(-\frac{\epsilon_s}{k_BT}\right), \qquad \Gamma_c = a_0 \ln\!\left(\frac{\sigma_s}{2H}\right). \tag{3}$$

Here ϵ_s is the effective ion–surface interaction energy, σ_s the ion–surface equilibrium distance, H the pore width, and a_0 an empirical geometric factor encoding the shape of the confinement-induced mobility profile; we find $a_0 \approx 3$ for neutral surfaces (van der Waals ionophilicity only) and $a_0 \approx 6$ for charged surfaces (additional electrostatic trapping within the electrical double layer). The pore-averaged diffusion coefficient for neutral pores is then

$$D_p = D_0[1 + 2\Gamma_c(1 - \Gamma_s)], \tag{4}$$

while for charged pores an electrostatic escape factor Γ_e modulates surface desorption via field-assisted barrier lowering (Poole–Frenkel effect) and correlation-induced mobility enhancement in the electrical double layer:

$$D_p = D_0[1 + 2\Gamma_c(1 - \Gamma_s\Gamma_e)]. \tag{5}$$

This decomposition is not merely heuristic but follows rigorously from dimensional analysis: applying the Buckingham Pi theorem to ion drift velocity under an external field naturally yields a governing function $f = 1 - \tilde{\sigma}_s f_B + \tilde{\sigma}_s f_s$, where the bulk deviation term $(1 - \tilde{\sigma}_s f_B)$ maps onto Γ_c and the interfacial term $\tilde{\sigma}_s f_s$ maps onto Γ_s. The logarithmic scaling with confinement and exponential dependence on surface energy thus represent the unique functional forms consistent with both molecular-scale physics and dimensional constraints. The framework recovers hydrodynamic confinement behavior in the weak-ionophilicity limit ($\Gamma_s \to 1$) while capturing the strong surface-chemistry and electrostatic dependencies observed in MD; plotting D_p against MD-derived diffusion coefficients for charged (Fig. S12e) and uncharged surfaces yields points close to the unity line across all pore widths, confirming quantitative theory–simulation agreement.

III. DIMENSIONAL ANALYSIS OF ION CONDUCTIVITY IN NANOPOROUS MEDIA:

We perform a dimensional analysis guided by the Buckingham Π-theorem to establish a rigorous foundation for the phenomenological framework in the previous sections and to identify the central dimensionless parameters governing ion transport in nanoporous media. The average ion drift velocity $\tilde{v}_d$ is taken to depend on the bulk self-diffusion coefficient D_0, ion concentration C_i, ion charge q_i, applied electric field E, pore width H, surface ionophilicity ϵ_s, ion–surface equilibrium distance σ_s, thermal energy k_BT, surface charge q_s, and medium permittivity $\epsilon_r\epsilon_0$:

$$\tilde{v}_d = f(E,\, D_0,\, H,\, \epsilon_s,\, \sigma_s,\, C_i,\, q_i,\, q_s,\, \epsilon_r\epsilon_0,\, k_BT). \tag{6}$$

With eleven dimensional parameters spanning four basis vectors, the theorem reduces the description to seven dimensionless groups. Recasting concentration via the Debye length $\lambda_D = \sqrt{\epsilon_0 k_BT/C_i q_i^2}$ yields

$$\frac{\tilde{v}_d\lambda_D}{D_0} = f\!\left(\frac{Eq_i\lambda_D}{k_BT},\, \frac{\sigma_s}{H},\, \frac{\lambda_D}{H},\, \frac{\epsilon_s}{k_BT},\, \frac{q_s}{E\epsilon_0\epsilon_r\lambda_D^2},\, \frac{q_iq_s}{\epsilon_0\epsilon_r\lambda_D k_BT}\right). \tag{7}$$

Invoking linear response in the limit of weak field and negligible surface charge, $\tilde{v}_d$ scales linearly with E, pulling the first argument outside f and recovering the Nernst–Einstein relation on the left-hand side (bulk limit f=1):

$$\frac{\tilde{v}_d k_BT}{Eq_iD_0} = f\!\left(\frac{\sigma_s}{H},\, \frac{\lambda_D}{H},\, \frac{\epsilon_s}{k_BT},\, \frac{q_s}{E\epsilon_0\epsilon_r\lambda_D^2},\, \frac{q_iq_s}{4\pi\epsilon_0\epsilon_r\lambda_D k_BT}\right). \tag{8}$$

Denoting $\tilde{\sigma}_s \equiv \sigma_s/H$, $\tilde{\lambda}_D \equiv \lambda_D/H$, and $\tilde{\epsilon}_s \equiv \epsilon_s/k_BT$: $\tilde{\sigma}_s$ captures confinement effects that grow significant only as H approaches the ion size; $\tilde{\lambda}_D$ characterizes double-layer overlap, which at 1 M varies from 0.3 to 0.03 as H increases

from 1 to 10 nm and can be safely neglected since overlap is negligible even at the narrowest pore [5–7]; $\tilde{\epsilon}_s$ encodes surface ionophilicity and hydrophilicity, relevant only when the surface-to-volume ratio is large. The fourth group, $q_s/E\epsilon_0\epsilon_r\lambda_D^2$, is the ratio of ion–surface electrostatic interaction energy to external field energy at the Debye scale. At the same time, the fifth, $q_i q_s/4\pi\epsilon_0\epsilon_r\lambda_D k_B T$, represents the thermal-energy-normalized cost for a surface ion to escape charge sites.

A. Functional Form from Dimensional Constraints

The functional form of f follows from requiring that ion transport decompose into bulk-like and interfacial contributions consistent with the discussion in the previous section:

$$f = 1 - \tilde{\sigma}_s f_B + \tilde{\sigma}_s f_s, \tag{9}$$

where (1 - $\tilde{\sigma}_s f_B$) captures the deviation of the bulk-like region from true bulk behavior and $\tilde{\sigma}_s f_s$ encapsulates interfacial contributions; the scaling with $\tilde{\sigma}_s$ is mandated by dimensional analysis, as mobility corrections must track the surface-to-volume ratio. Inspired by the asymptotic developments of Simonnin et al. [3] and Saugey *et al.* [4] and validated by MD (Fig. S12), we adopt

$$f_B = -a_0 \ln(\tilde{\sigma}_s/2), \tag{10}$$

where the logarithmic form captures the algebraic decay of hydrodynamic correlations under confinement, consistent with long-wavelength mode suppression in slit geometries, and a_0 is a fitting parameter determined from experiment or simulation. The interfacial term takes the form

$$f_s = f_B \exp(-\tilde{\epsilon}_s), \tag{11}$$

where the Boltzmann factor governs ion desorption from an uncharged surface; this exponential dependence on surface binding energy is the unique form consistent with activated escape from interfacial traps and maps directly onto the surface factor $\Gamma_s = \exp(-\tilde{\epsilon}_s)$ derived in previous sections. Substituting into the drift velocity and identifying $\Gamma_c \equiv a_0 \ln(\tilde{\sigma}_s/2)$ and $\Gamma_s \equiv \exp(-\tilde{\epsilon}_s)$ yields

$$\tilde{v}_d = \frac{n q_i E}{k_B T} D_0 [1 + 2\Gamma_c(1 - \Gamma_s)]\,, \tag{12}$$

where the prefactor n reflects diffusivity anisotropy due to severely restricted perpendicular transport (n=2/3 for H>1 nm; n=1/3 for $H \leq 1$ nm). This expression is mathematically equivalent to the diffusion coefficient framework discussed earlier, confirming that the same physics governs both equilibrium diffusion and field-driven transport, and that the convergence of dimensional analysis, activation energy theory, and hydrodynamic scaling validates the framework's predictive robustness across diverse nanopore conditions.

IV. ION HYDRATION STATE AND WATER RESIDENCE TIME ANALYSIS

Coordination numbers (CN) between Na^+ and water oxygen were computed by integrating the Na–O_w radial distribution function to its first minimum at $r_{\min}$=0.33 nm,

$$CN = 4\pi\rho_{O_w} \int_0^{r_{\min}} g_{\text{Na-O}_w}(r)\, r^2\, dr, \tag{13}$$

where ρ_{O_w} is the water-oxygen number density within 0.4 nm of the surface, with RDFs computed separately for each surface and averaged. Water mean residence times τ_m were extracted from the continuous survival probability

$$P(t) = \frac{1}{T}\sum_{i=1}^{T} \frac{N(t)}{N(0)}, \qquad \tau_m = \int_0^{\infty} P(t)\, dt, \tag{14}$$

evaluated over $\tau_{\max}$=1800 ps using 2000 trajectory frames, where $N(t)$ is the number of water molecules remaining in the interfacial region at time t.

Figure S3 reveals fundamentally different hydration dynamics on neutral versus charged surfaces. On neutral surfaces (Figs. S3a, c), interfacial Na^+ CN increases minimally from 4.60 to 4.85 with ionophilicity, well below the bulk

value of 5.9; while residence times remain short (15–54 ps), indicating dynamic, weakly bound hydration shells with rapid interfacial-bulk exchange despite partial dehydration. On charged surfaces (Figs. S3b, d), CN rises from 4.70 to 5.35, approaching bulk hydration, while residence times increase by nearly two orders of magnitude—from $\sim$ 70 ps at low charge to $\sim$ 600 ps at Σ_s=2.0 e/nm^2 and high ionophilicity—reflecting electrostatic kinetic trapping of water at the interface that suppresses bulk exchange and stabilizes long-lived hydration structures. These persistent hydration networks underpin the correlated ion–water transport and interfacial superionicity discussed earlier. Collectively, neutral surfaces favor partially dehydrated, inner-sphere-like Na^+ complexes with fast exchange, whereas charged ionophilic surfaces stabilize predominantly outer-sphere complexes with long-lived hydration shells.

V. ION HOPPING MODEL ON CHARGED MINERAL SURFACES:

Adapting the Poole–Frenkel theory of trap-limited electron conduction in semiconductors to charged dielectric nanopores, the applied electric field reduces the ion escape barrier by

$$\Delta U = q_i r E \cos\theta + \frac{q_i q_s}{4\pi\epsilon_0\epsilon_r r}, \tag{15}$$

where the first term is the field contribution and the second is the unscreened ion–surface electrostatic attraction. This barrier is maximized at $r_{\max} = \sqrt{q_s/4\pi\epsilon_0\epsilon_r E\cos\theta}$, giving the barrier-lowering energy

$$U_H = \sqrt{\frac{q_i^2 q_s E\cos\theta}{\pi\epsilon_0\epsilon_r}}, \tag{16}$$

which corresponds to the Hartke three-dimensional Poole–Frenkel formulation [8] that accommodates unequal ion and surface charges and allows ion hopping at angle $\theta \in [0, \pi/2]$ relative to $\mathbf{E}$. At low ionophilicity $\theta \to \pi/2$, accounting for the slight nonlinearity in drift curves, while at high ionophilicity $\theta \to 2\pi/5$, reflecting a tangential hopping component. The total escape barrier is $U_B - U_H$, where

$$U_B \approx \frac{q_i q_s}{4\pi\epsilon_0\epsilon_r r_0}$$

is the ion binding energy to the trap, with r_0 (the effective double-layer size, ranging from $1.5\sigma_s$ to $4\sigma_s$ as ionophilicity decreases) setting the trap depth. The ion hopping rate out of surface charge traps is thus

$$\Gamma_e = \exp\left(-\frac{U_B - U_H}{k_B T}\right), \tag{17}$$

which modulates the adsorption–desorption kinetics encoded in Γ_s, yielding the drift velocity for charged nanopores:

$$\tilde{v}_d = \frac{n q_i E}{k_B T} D_0 [1 + 2\Gamma_c(1 - \Gamma_s\Gamma_e)]\,. \tag{18}$$

A. Simulation Evidence for Hopping Dynamics

The self-part of the Van Hove correlation function $G_s(r,t)$, measuring the probability of an ion displacing by r in time t, directly reveals the crossover from continuous diffusion on neutral surfaces to intermittent hopping on charged ones. On neutral surfaces (left columns, Figs. S5–S6), $G_s(r,t)$ remains nearly Gaussian at all fields; a single symmetric peak shifting smoothly to larger r, confirming unobstructed drift-diffusion and demonstrating that van der Waals interactions alone, even at high ionophilicity, produce no appreciable trapping. On charged surfaces with $\Sigma_s \geq 0.5$ e/nm^2 (middle and right columns), pronounced non-Gaussian features emerge: secondary peaks and shoulders at later times signal rapid hops between neighboring charge sites separated by periods of electrostatic trapping, with signatures strengthening monotonically with Σ_s; dashed vertical lines mark the characteristic hopping distances set by the mean inter-charge spacing. At Σ_s=2.0 e/nm^2, $G_s(r,t)$ becomes distinctly multimodal, with well-separated peaks corresponding to one, two, or three successive hops between trap sites at inter-trap distances $\Delta \approx 0.3$–0.5 nm, confirming sequential thermally activated escape consistent with the Poole–Frenkel hopping picture. Comparing low (ϵ_s/k_BT=0.07, Fig. S5) and high (ϵ_s/k_BT=0.58, Fig. S6) ionophilicity reveals the cooperative role of dispersion forces: at low ionophilicity, non-Gaussian features appear only at the largest Σ_s and decay rapidly, whereas high ionophilicity produces more pronounced and longer-lived secondary peaks, reflecting deeper traps and slower escape consistent with the $\Gamma_s\Gamma_e$ factor in the drift-velocity model. Collectively, these Van Hove analyses provide microscopic evidence for the diffusion-to-hopping crossover and motivate the explicit inclusion of field-assisted barrier lowering (U_H) and activated-escape dynamics (Γ_e) in the conductivity theory of charged nanopores.

VI. CORRELATED ION DRIFT AT THE INTERFACE:

The classical Poole–Frenkel formalism assumes uncorrelated trap sites and becomes increasingly inaccurate at high surface charge densities and strong fields, where we observe interfacial superionicity; surface ions drifting faster than those in the bulk-like region. We rationalize this via an extended Poole–Frenkel theory incorporating correlation effects: as in superionicity in crystals [9], elevated interfacial ion density reduces the escape barrier through charge–charge and charge–dipole interactions. PMF profiles at Σ_s=2.0 e/nm^2 and zero field (Figs. S7a, b) confirm barrier screening by adsorbed ions, with higher ionophilicity (ϵ_s/k_BT=0.58) further raising local ion density ρ_s and lowering U_B. We quantify the excess correlation energy U_C in a cluster of n dipoles and m net site charges as

$$U_C = \sum_{i=1}^{n} \frac{pq}{4\pi\epsilon_0\Delta_i^2} + \sum_{j=1}^{m} \frac{q^2}{4\pi\epsilon_0\Delta_j} \approx \frac{cq^2}{4\pi\epsilon_0\Delta}, \tag{19}$$

where Δ is the inter-trap distance, p the adsorption-induced dipole, and c a geometric tuning factor. Under strong applied fields, escaping cations perturb the local field of neighboring surface ions; leveraging a Taylor expansion, this electrostatic perturbation energy is

$$U_P = \frac{q^2\delta(E)}{4\pi\epsilon_0\Delta^2}, \tag{20}$$

where $\delta(E)$ is the ballistic hopping distance along $\mathbf{E}$, confirmed by PMF profiles under applied fields at ϵ_s/k_BT=0.58 (Figs. S7c, d). Summing over all clusters in the canonical ensemble, the total correlation energy is

$$U_{\text{corr}} = \sum_{i=1}^{n_{cl}} P_i \left\{ \frac{c_i q^2}{4\pi\epsilon_0\Delta} + \frac{q^2\delta_i(E)}{4\pi\epsilon_0\Delta^2} \right\}, \tag{21}$$

where P_i is the probability of forming a cluster of size i. In the high-density, high-field limit where large cation chains percolate across the surface, this simplifies to

$$U_{\text{corr}} = \frac{q^2 G(\rho_s, \rho_{cr})}{4\pi\epsilon_0\Delta} \left\{ c^\infty + G(E, E_{cr}) \frac{\delta^\infty}{\Delta} \right\}, \tag{22}$$

where G is a sigmoid transition function ($\Delta\rho$=0.5, ΔE=0.2) delineating the crossover from uncorrelated to correlated drift, and ρ_{cr}, E_{cr} are the critical density and field at correlation onset. The asymptotic parameters c^∞ and δ^∞ are extracted from percolation-based fits to MD data (Table S1); future refinements should replace these with physics-based parameterizations via direct cluster enumeration, trajectory-based $\delta(E)$ extraction, and percolation scaling theory for G. The surface ion density ρ_s is computed via the correlation-hole approach, which overcomes Poisson–Boltzmann limitations at high surface charge [10]. Incorporating U_{corr}, the hopping rate generalizes to

$$\Gamma_e = \exp\left(-\frac{U_B - \Delta U_{\max} - U_{\text{corr}}}{k_BT} \right), \tag{23}$$

reducing to the uncorrelated case (Equation 18) as $U_{\text{corr}} \to 0$. Velocity distributions (Fig. S9) confirm that enhanced surface mobility arises exclusively on charged ionophilic interfaces—absent for neutral pores, minimal at ϵ_s/k_BT=0.07, and superionic at ϵ_s/k_BT=0.58, underscoring the necessity of both Poole–Frenkel barrier lowering and high-ρ_s correlations.

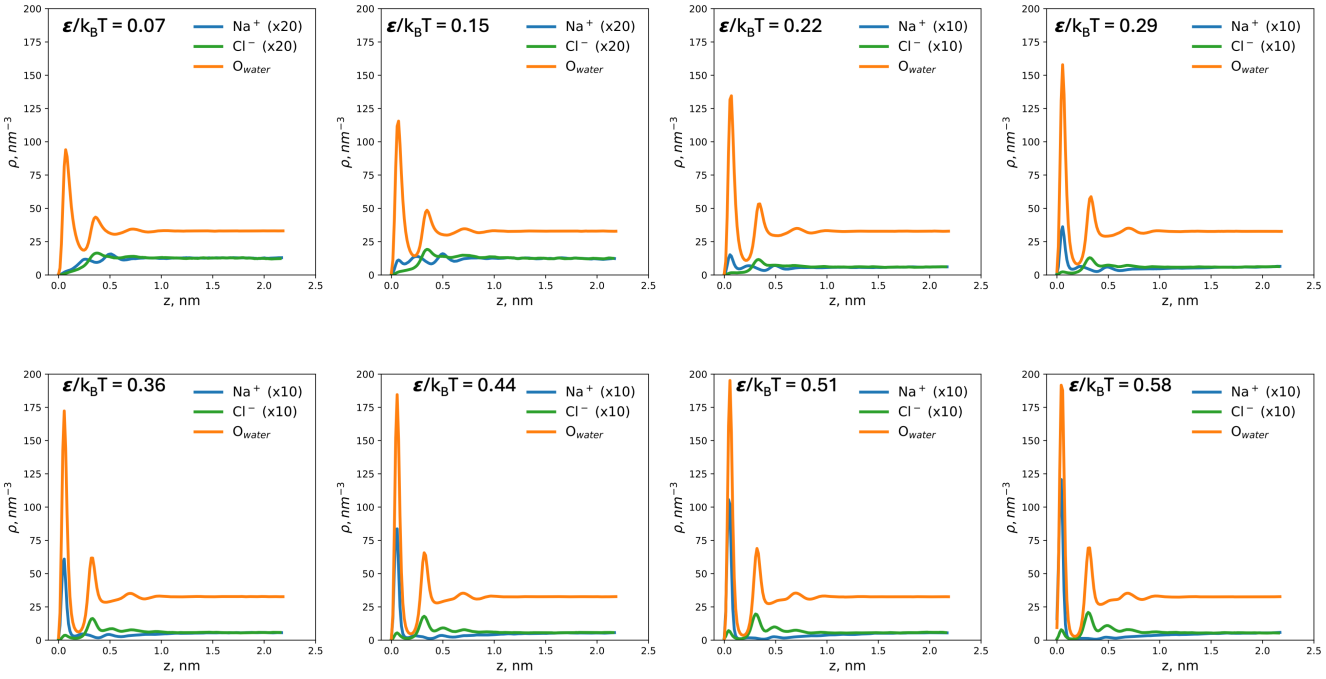

FIG. S1. Density profiles of Na^+, Cl^-, and water oxygen atoms in neutral nanopores as a function of distance from the surface for varying surface ionophilicity ϵ_s/k_BT. Ion densities are scaled for visibility as indicated in the legends.

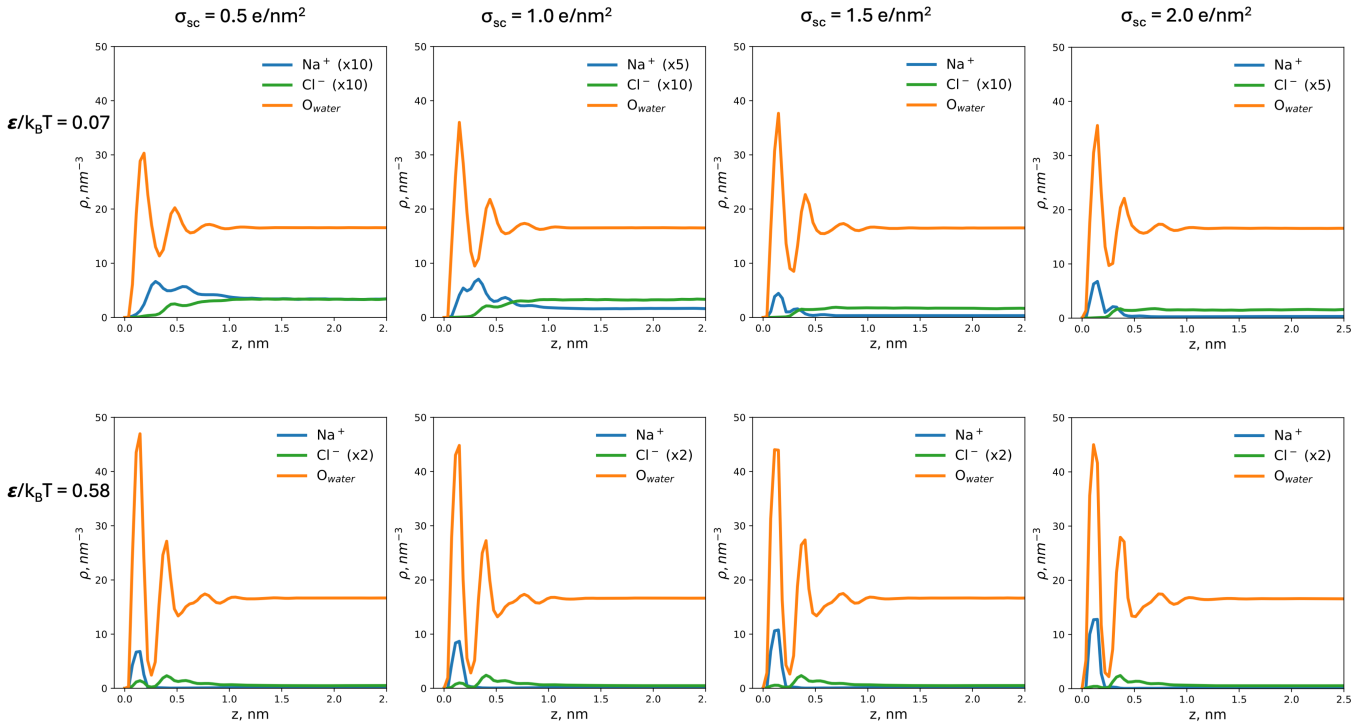

FIG. S2. Density profiles of Na^+, Cl^-, and water oxygen atoms in charged nanopores for two ionophilicity levels (ϵ_s/k_BT=0.07 and 0.58) across surface charge densities Σ_s from 0.5 to 2.0 e/nm^2. Ion densities are scaled for visibility as indicated in the legends.

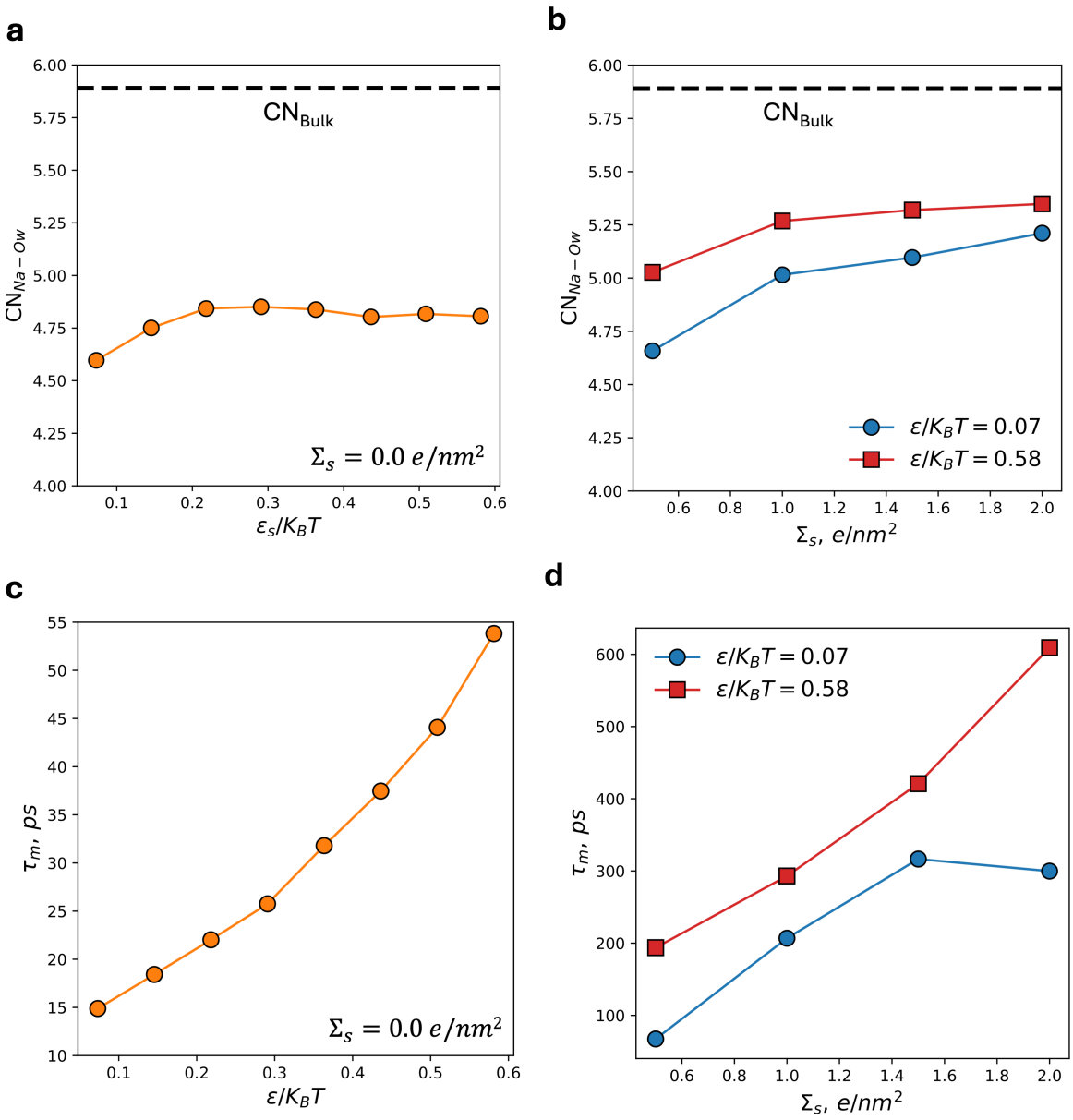

FIG. S3. **Ion hydration and water exchange dynamics on neutral and charged interfaces.** (**a**) Na^+-Ow coordination number at neutral surfaces increases minimally from 4.60 to 4.85 with ionophilicity, remaining below bulk CN=5.9 (dashed line). (**b**) On charged surfaces, CN approaches bulk values as surface charge and ionophilicity increase. (**c**) Water residence times on neutral surfaces are short (15-54 ps), indicating rapid interfacial-bulk exchange. (**d**) Charged surfaces exhibit residence times 100 times longer (70-600 ps), demonstrating kinetic trapping of water that suppresses exchange and stabilizes hydration structures essential for correlated transport.

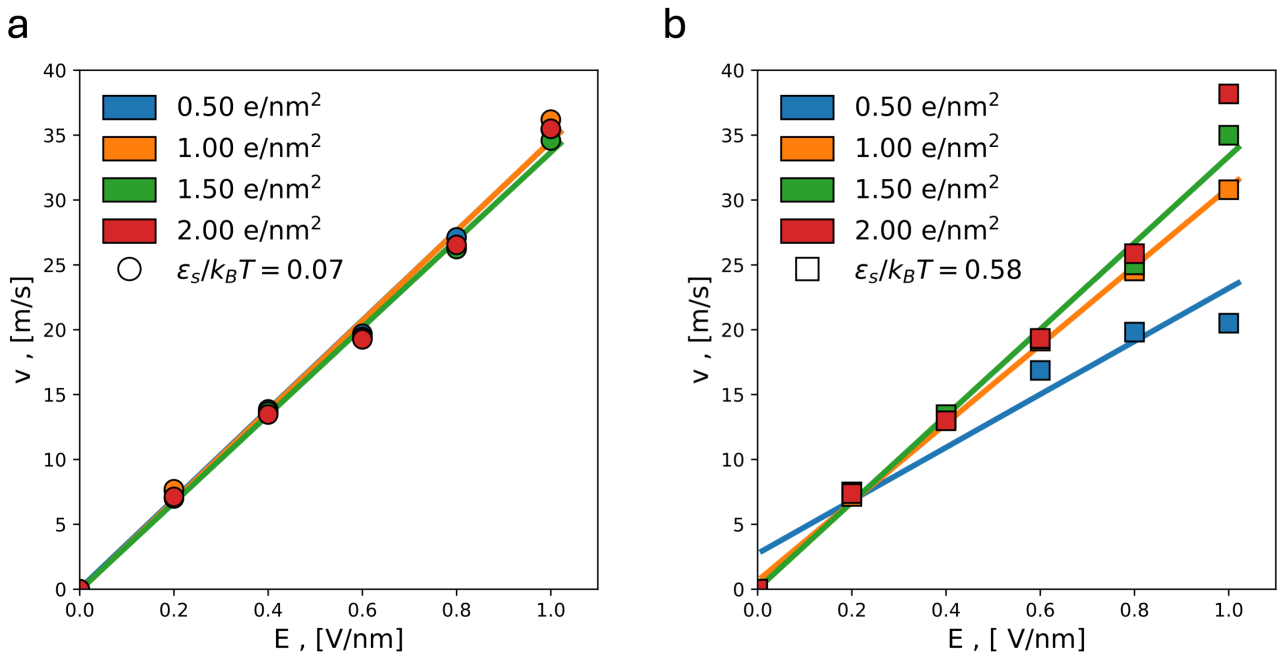

FIG. S4. Drift velocity versus electric field for Cl^- shows linear dependence at Σ_s=0.5-2.0 e/nm^2 ($\epsilon_s^* = 0.07$ in panel **a**, 0.58 in panel **b**)

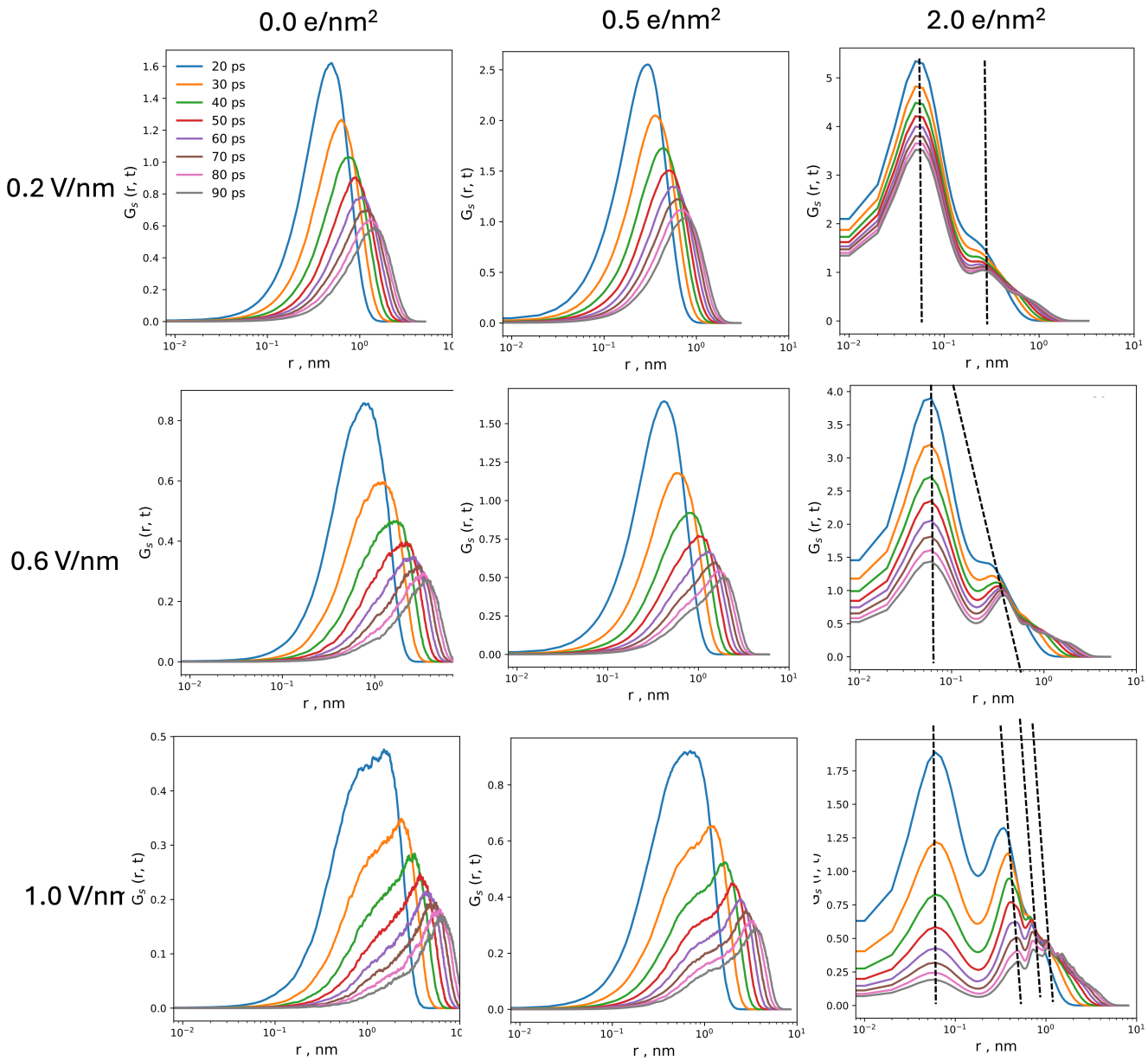

FIG. S5. Self part of the Van Hove correlation function for Na^+ in neutral and charged nanopores at ϵ_s/k_BT=0.07, showing pronounced non-Gaussian features and clear hopping signatures at high surface charge, in contrast to the nearly Gaussian, diffusive behavior in neutral pores.

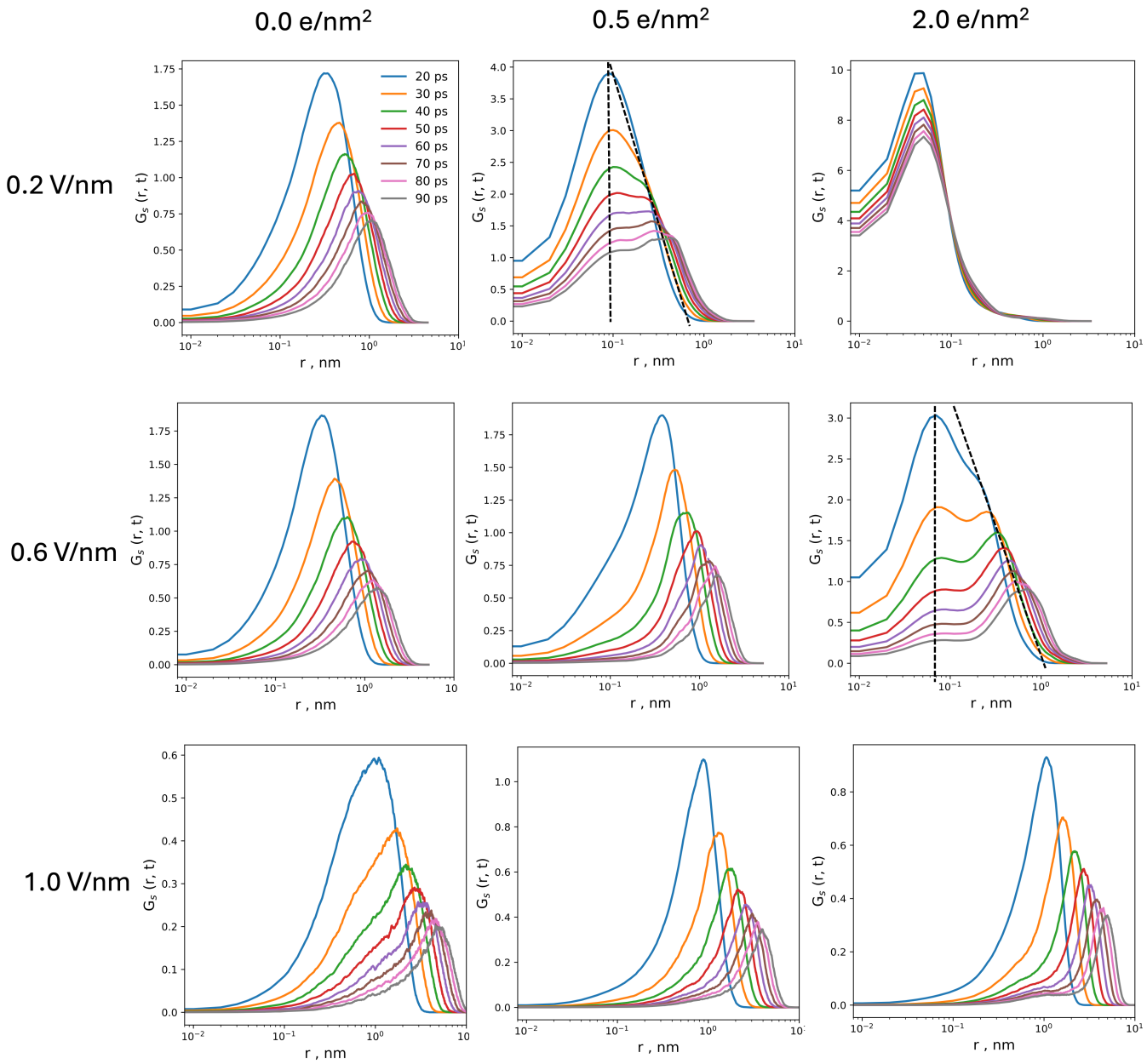

FIG. S6. Self part of the Van Hove correlation function for Na^+ in neutral and charged nanopores at ϵ_s/k_BT=0.07, demonstrating strong hopping peaks and enhanced intermittency at high surface charge, while neutral pores retain a more diffusive profile despite increased ionophilicity

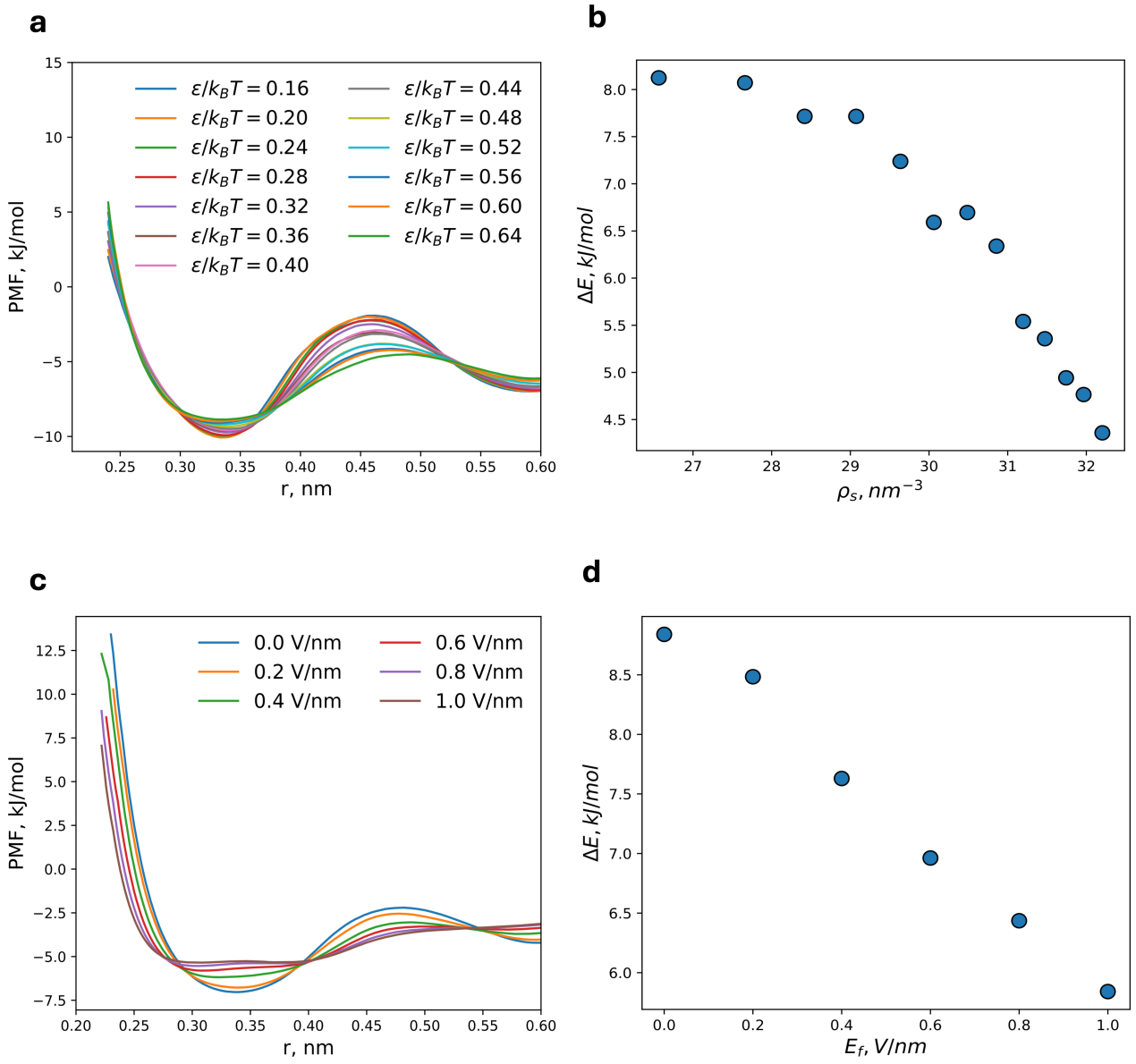

FIG. S7. **Approximate free-energy barriers for Na^+ hopping from surface traps on highly charged nanopores with surface charge density Σ_s=2.0 e/nm^2:** (**a**) effective potential profiles showing barrier lowering driven solely by charge–charge and charge–dipole interactions as surface ion clusters accumulate, in the absence of an applied electric field; (**b**) corresponding decrease of the escape barrier height as a function of cluster density at the interface; (**c**) field-assisted Poole–Frenkel–type barrier lowering for a fixed interfacial ion configuration under increasing external electric field; and (**d**) resulting reduction of the energy barrier with electric field strength, highlighting the cooperative role of interfacial correlations and the applied field in promoting ion escape from surface traps.

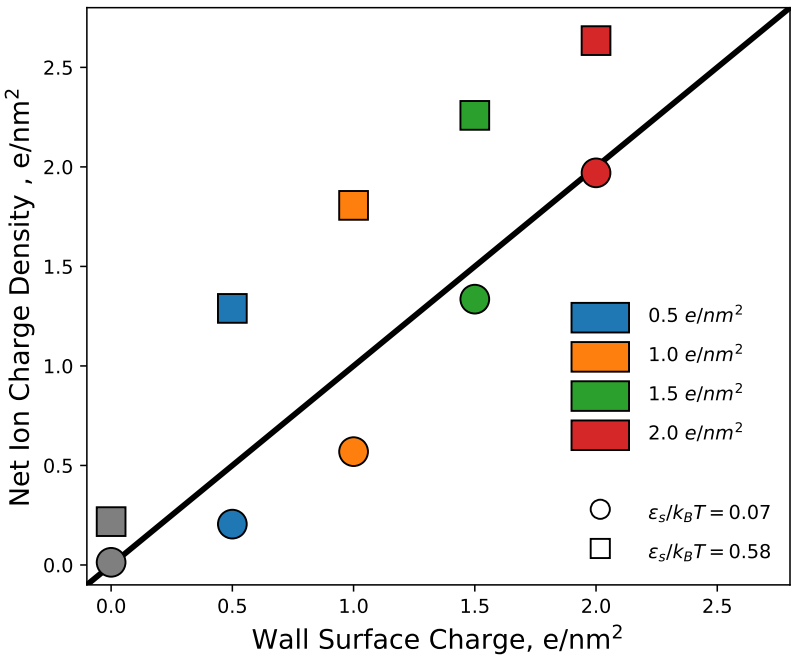

FIG. S8. Net ion charge density at the nanopore surface versus wall surface charge Σ_s for high (ϵ_s/k_BT=0.07, circles) and low (ϵ_s/k_BT=0.58, squares) ionophilicity. The diagonal line indicates perfect charge compensation; points above the line indicate overscreening, and points below the line indicate underscreening.

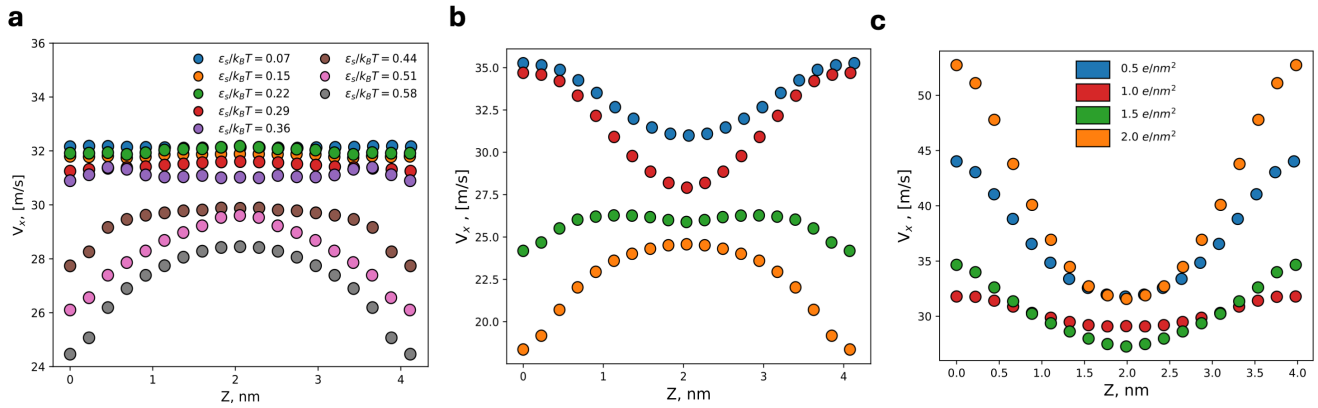

FIG. S9. Velocity distributions of Na^+ in nanopores for (**a**) a neutral surface, (**b**) a highly ionophilic charged surface with ϵ_s/k_BT=0.07, and (**c**) a weakly ionophilic charged surface with ϵ_s/k_BT=0.58, indicating that interfacial velocity enhancement and superionic-like drift are mainly associated with highly charged, strongly ionophilic interfaces rather than neutral pores.

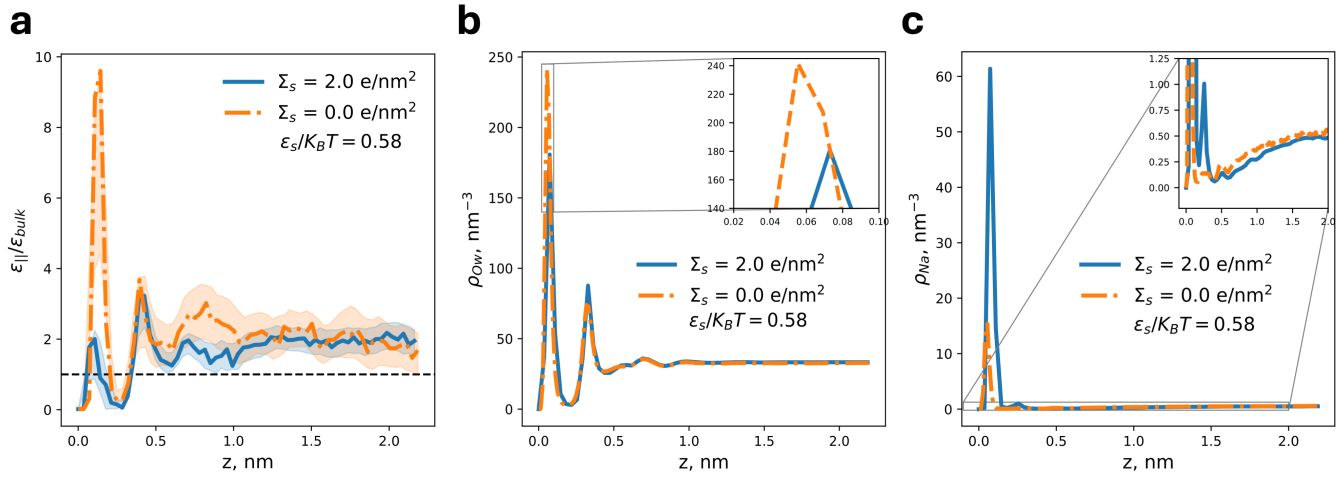

FIG. S10. **In-plane dielectric permittivity and structural profiles confirm that interfacial superionicity is driven by concerted ion migration rather than dielectric enhancement.** Panel (**a**) shows in-plane dielectric permittivity profiles, panel (**b**) shows water oxygen density profiles, and panel (**c**) shows Na^+ density profiles. All panels compare a charged surface (Σ_s=2.0 e/nm^2) against a neutral surface at identical ionophilicity (ϵ_s/K_BT=0.58). Despite the neutral surface exhibiting higher near-surface $\varepsilon_{||}$, superionicity is observed only on the charged surface. Dense Na^+ accumulation on the charged surface suppresses $\varepsilon_{||}$ through ion crowding and displacement of interfacial water. This demonstrates that concerted ion migration through percolation networks is the primary driver of interfacial superionicity, not dielectric enhancement.

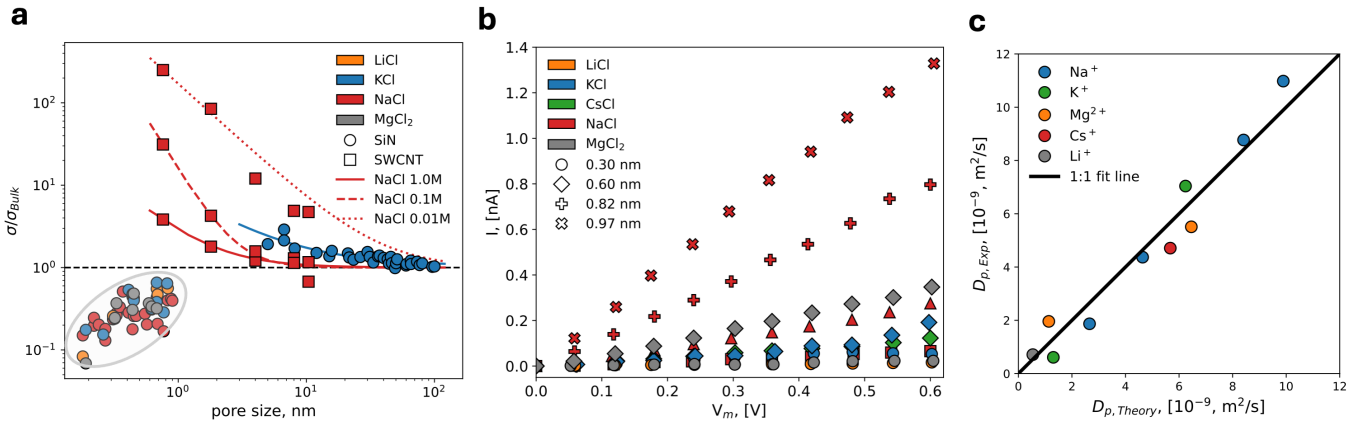

FIG. S11. **Experimental conductivity, current–voltage, and diffusion coefficient data for nanopore systems**. (**a**) Normalized conductivity versus pore size for LiCl, NaCl, KCl, and $MgCl_2$ in silicon nitride nanopores [11–13] and single-walled carbon nanotubes [14]. Solid and dashed lines show NaCl conductivity at 1.0, 0.1, and 0.01 M. (**b**) Current–voltage curves for sub-nanometer silicon nitride nanopores from Rigo *et al.* [13] across pore diameters of 0.30, 0.60, 0.82, and 0.97 nm for LiCl, KCl, CsCl, NaCl, and $MgCl_2$ electrolytes. (**c**) Experimentally extracted pore diffusion coefficients $D_{p,\,Exp}$ vs. theoretical predictions $D_{p,\,Theory}$ for Na^+, K^+, Mg^{2+}, Cs^+, and Li^+. The black line denotes the 1:1 reference.

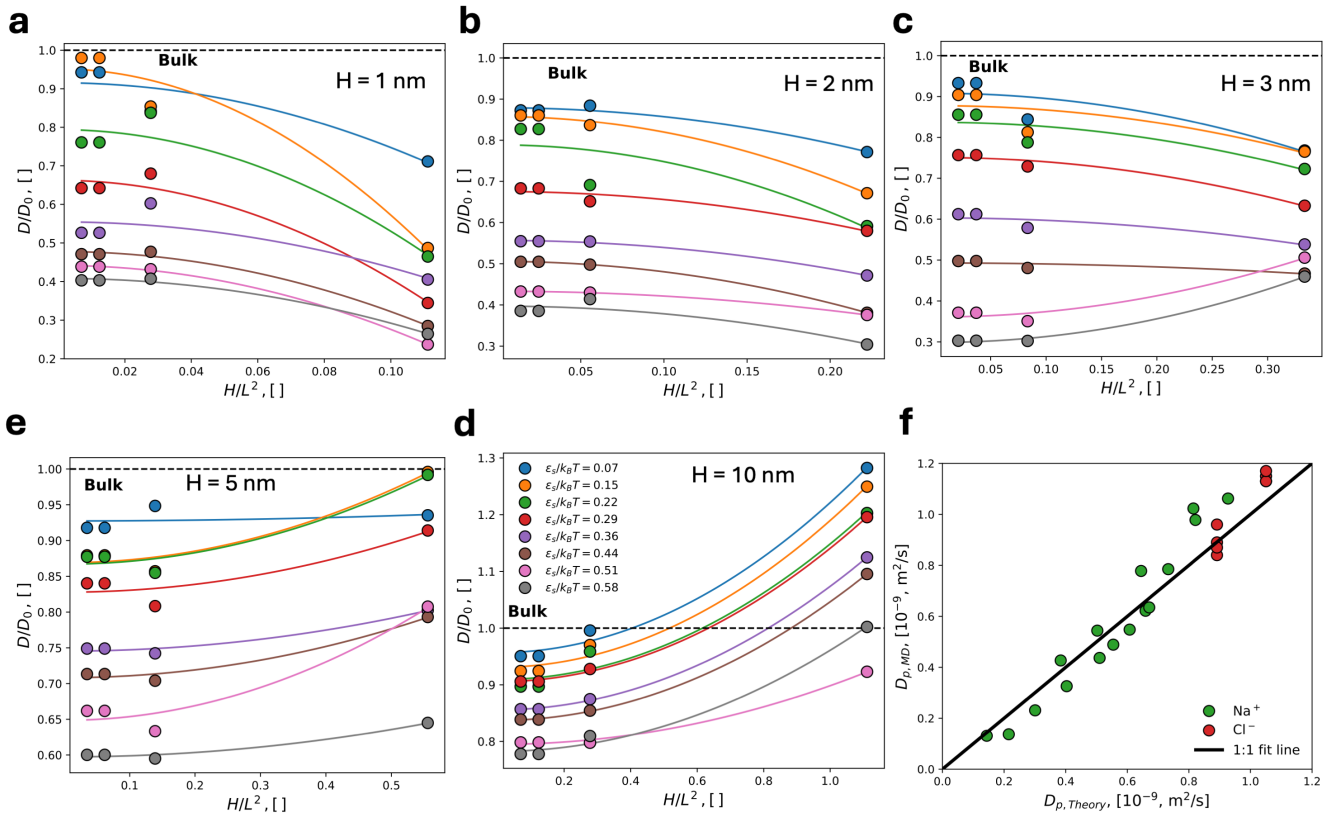

FIG. S12. Na^+ diffusion coefficients as a function of pore width and surface ionophilicity in neutral nanopores (**a**–**b**), together with theoretical prediction and MD data for charged nanopores at fixed surface charge density in panel (**f**), all corrected for finite system size to obtain the diffusion coefficient in the infinite-system limit.

TABLE S1. **Percolation-model fitting parameters c^{∞} and δ^{∞} used to evaluate the correlation energy U_{corr} as a function of surface ionophilicity ϵ_s/k_BT, surface charge density, and pore size (5 and 10 nm) in the correlated ion-drift model**.

ϵ_s/k_BT	Charge (e/nm^2)	5 nm		10 nm	
		c^{∞}	δ^{∞}	c^{∞}	δ^{∞}
	0.5	0.260	0.067	0.471	0.172
	1.0	0.294	0.090	0.577	0.202
	1.5	0.335	0.121	0.713	0.207
0.07	2.5	0.416	0.135	0.890	0.218
	0.5	0.142	0.118	0.189	0.351
	1.0	0.040	0.187	0.218	0.377
	1.5	0.022	0.344	0.195	0.752
0.58	2.0	0.166	0.446	0.473	0.778

TABLE S2. **Lennard-Jones ϵ parameters for Na–surface, Cl–surface, and Ow–surface interactions used in the reduced-complexity model (in kJ/mol), with ion–surface LJ diameters $\sigma_{\text{Na-s}}$=0.27 nm, $\sigma_{\text{Cl-s}}$=0.31 nm, and $\sigma_{\text{Ow-s}}$=0.27 nm**.

	$\epsilon_{\text{Na-s}}$	$\epsilon_{\text{Cl-s}}$	$\epsilon_{\text{Ow-s}}$
1.	0.182125	0.088375	0.205000
2.	0.363250	0.175750	0.290000
3.	0.544375	0.263125	0.375000
4.	0.725500	0.350500	0.460000
5.	0.906625	0.437875	0.545000
6.	1.087750	0.525250	0.630000
7.	1.268875	0.612625	0.715000
8.	1.450000	0.700000	0.800000

VII. REFERENCES

[1] Z. A. Goodwin and A. A. Kornyshev, Underscreening, overscreening and double-layer capacitance, Electrochemistry Communications **82**, 129 (2017).

[2] S. S. Lee, A. Koishi, I. C. Bourg, and P. Fenter, Ion correlations drive charge overscreening and heterogeneous nucleation at solid–aqueous electrolyte interfaces, Proceedings of the National Academy of Sciences **118**, e2105154118 (2021).

[3] P. Simonnin, B. Noetinger, C. Nieto-Draghi, V. Marry, and B. Rotenberg, Diffusion under confinement: Hydrodynamic finite-size effects in simulation, Journal of chemical theory and computation **13**, 2881 (2017).

[4] A. Saugey, L. Joly, C. Ybert, J.-L. Barrat, and L. Bocquet, Diffusion in pores and its dependence on boundary conditions, Journal of Physics: Condensed Matter **17**, S4075 (2005).

[5] D. Stein, M. Kruithof, and C. Dekker, Surface-charge-governed ion transport in nanofluidic channels, Physical Review Letters **93**, 035901 (2004).

[6] Y. Green, Ion transport in nanopores with highly overlapping electric double layers, The Journal of Chemical Physics **154** (2021).

[7] R. B. Schoch, J. Han, and P. Renaud, Transport phenomena in nanofluidics, Reviews of modern physics **80**, 839 (2008).

[8] J. Hartke, The three-dimensional poole-frenkel effect, Journal of Applied Physics **39**, 4871 (1968).

[9] X. He, Y. Zhu, and Y. Mo, Origin of fast ion diffusion in super-ionic conductors, Nature communications **8**, 15893 (2017).

[10] A. Goyal, I. Palaia, K. Ioannidou, F.-J. Ulm, H. Van Damme, R. J.-M. Pellenq, E. Trizac, and E. Del Gado, The physics of cement cohesion, Science advances **7**, eabg5882 (2021).

[11] D. C. Martinez Casillas, M. P. Longinotti, M. M. Bruno, F. Vaca Chavez, R. H. Acosta, and H. R. Corti, Diffusion of water and electrolytes in mesoporous silica with a wide range of pore sizes, The Journal of Physical Chemistry C **122**, 3638 (2018).

[12] S. W. Kowalczyk, A. Y. Grosberg, Y. Rabin, and C. Dekker, Modeling the conductance and dna blockade of solid-state nanopores, Nanotechnology **22**, 315101 (2011).

[13] E. Rigo, Z. Dong, J. H. Park, E. Kennedy, M. Hokmabadi, L. Almonte-Garcia, L. Ding, N. Aluru, and G. Timp, Measurements of the size and correlations between ions using an electrolytic point contact, Nature communications **10**, 2382 (2019).

[14] S. Balme, F. Picaud, M. Manghi, J. Palmeri, M. Bechelany, S. Cabello-Aguilar, A. Abou-Chaaya, P. Miele, E. Balanzat, and J. M. Janot, Ionic transport through sub-10 nm diameter hydrophobic high-aspect ratio nanopores: experiment, theory and simulation, Scientific reports **5**, 10135 (2015).